

ACCEPTED MANUSCRIPT

Consistent optical surface inspection based on open environment droplet size-controlled condensation figures

To cite this article before publication: Jingyang Yan *et al* 2021 *Meas. Sci. Technol.* in press <https://doi.org/10.1088/1361-6501/ac0d24>

Manuscript version: Accepted Manuscript

Accepted Manuscript is “the version of the article accepted for publication including all changes made as a result of the peer review process, and which may also include the addition to the article by IOP Publishing of a header, an article ID, a cover sheet and/or an ‘Accepted Manuscript’ watermark, but excluding any other editing, typesetting or other changes made by IOP Publishing and/or its licensors”

This Accepted Manuscript is © 2021 IOP Publishing Ltd.

During the embargo period (the 12 month period from the publication of the Version of Record of this article), the Accepted Manuscript is fully protected by copyright and cannot be reused or reposted elsewhere.

As the Version of Record of this article is going to be / has been published on a subscription basis, this Accepted Manuscript is available for reuse under a CC BY-NC-ND 3.0 licence after the 12 month embargo period.

After the embargo period, everyone is permitted to use copy and redistribute this article for non-commercial purposes only, provided that they adhere to all the terms of the licence <https://creativecommons.org/licenses/by-nc-nd/3.0>

Although reasonable endeavours have been taken to obtain all necessary permissions from third parties to include their copyrighted content within this article, their full citation and copyright line may not be present in this Accepted Manuscript version. Before using any content from this article, please refer to the Version of Record on IOPscience once published for full citation and copyright details, as permissions will likely be required. All third party content is fully copyright protected, unless specifically stated otherwise in the figure caption in the Version of Record.

View the [article online](#) for updates and enhancements.

Consistent optical surface inspection based on open environment droplet size-controlled condensation figures

Jingyang Yan¹, Rui Ma² and Xian Du¹

¹ Mechanical & Industrial Engineering Department, University of Massachusetts, Amherst, MA, USA

² Electrical & Computer Engineering Department, University of Massachusetts, Amherst, MA, USA

E-mail: xiandu@umass.edu

Abstract

Condensation figure (CF) is a simple and cost-effective method to inspect patterns and defects on product surfaces. This inspection method is based on energy differentials on surfaces. Due to wettability contrast, water droplets are preferentially nucleated and grown on hydrophilic regions. The formed CF can further be segmented for the recognition and measurement of the patterns on the surfaces. The state-of-the-art CF methods are close-environmental, while controlled open-environmental CF has broader applications in manufacturing and quality inspection. The lack of open-environmental CF for such applications is mostly because of the unavailable droplet size control methods. In this paper, we designed a high-resolution optical surface inspection system based on open environment droplet-size-controlled CFs. This is done by real-time imaging and recognizing the condensed droplet sizes and densities on surfaces, and accordingly tuning the vaporization and evaporation of droplets on the surface by the vapor flow rate. Our experimental results show that the average diameter of droplets can be controlled below 3.5 μm in a laboratory setup for different metal substrates. We also test the system for inspecting self-assembled monolayer patterns with linewidth of 5 μm on a gold surface; this can be promisingly used for online quality monitoring and in-process control of printed patterns in flexible devices manufacturing.

Keywords: Consistent condensation figures, droplet size control, machine vision, surface inspection

1. Introduction

Condensation figures (CFs) can be used to inspect surfaces with energy differentials. Because of wettability differences and wettability contrast on surfaces, water droplets are preferentially nucleated and grown on the hydrophilic regions. The formed CFs on surfaces can be further segmented for pattern recognition and measurement. CFs offer a simple, nondestructive, and cost-effective imaging method for surface inspection that may not be accessible by other techniques [1].

CFs, also called “breath figures”, have been applied for a variety of surface inspection tasks. In [2], CFs are used to inspect features of self-assembled monolayers (SAMs) of

multiple alkanethiolates on gold surfaces. The wettability contrast of SAMs and gold surfaces makes it possible to use the distribution of water droplets observed by optical microscopy to classify and measure the SAM patterns on the surfaces. A vapor-condensation-assisted (VCA) optical microscopy for ultralong carbon nanotubes (CNTs) and other nanostructures are developed in [3]. The VCA optical microscopy has two working mechanisms for CNT inspection. For CNTs with impurities, the warm water vapor is more likely to condense on the impure CNTs than the substrate. The condensed microdroplets of water work as scattering centers, appearing as bright dots under the dark-field microscope that sketch the outlines of CNTs. For clean CNTs, the substrate is

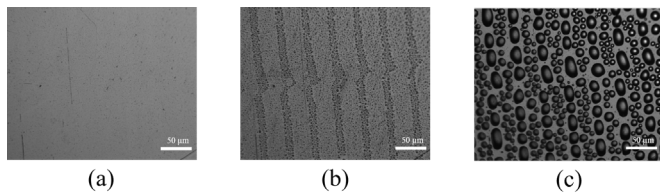


Fig. 1. Motivation of applying CFs and droplet size control for surface inspection. (a) Gold substrate under an optical microscope which is patterned with SAMs. (b) CF of patterned SAMs which shows the defect in the printing process. (c) Large droplets on the substrate which make the patterns undistinguishable.

treated with argon plasma which makes the substrate hydrophilic. When the warm water vapor continuously flows onto the substrate surface, the condensation droplets will gradually grow larger and merge into water films separated by CNTs since CNTs are hydrophobic, thus making CNTs distinguishable from the substrate. In [4], a VCA optical microscopy was adopted to visualize graphene on various substrates. Since the monolayer graphene-covered surface and uncovered surface have different wettability, these surfaces can be distinguished under the designed VCA optical microscopy. The authors also found that the VCA images can distinguish monolayer graphene from multilayer graphene. In [5], CFs were used for anti-counterfeiting. Si wafers and mirrors were treated with oxygen plasma to achieve hydrophilicity. Then, SAMs patterns were fabricated on the hydrophobic substrates. The SAMs patterns can thus be visible in CFs under human breath. In [6], a real-time CF system was presented for inspection and quality control of printed SAM patterns on a moving web in roll-to-roll microcontact printing processes. This imaging system can achieve pattern resolution up to 0.7 μm for patterned SAMs on gold.

The state-of-the-art CF methods, however, lack consistent droplet size control which can cause inaccurate and unstable CFs and thus misleading surface inspection results. All these CF methods rely on the natural growth of CFs, for which the droplets will keep growing during the inspection process. For most applications, e.g., microcontact printing [6], the size of printed patterns is micron-scale. If the droplets keep growing naturally without control, large droplets will make the printed patterns indistinguishable from the substrate.

In the following, we use Fig. 1 to further illustrate our motivations for consistent CF control. Figure 1(a) is the thiol pattern on the gold surface from a microcontact printing process. The patterned SAMs are invisible because the very thin monolayer has an insufficient thickness to differentiate the light reflectance from the thiol and gold patterns. Fortunately, the presence of thiol SAMs on the surface of metal creates a significant surface energy differential. A humid atmosphere can cause printed patterns to be visible on the CFs of the product due to this SAM-metal surface energy differential. When droplet size is appropriately controlled, as shown in Fig. 1(b), distortion is clearly visible in the middle of designated straight lines, which indicates faults occurring in the printing process. Without consistent CF control, as shown in Fig. 1(c), distortion is not clear for inspection because the

growing droplets dominate the printed pattern. Hence, the precise control of droplet size in CFs will facilitate the print pattern recognition and inspection with higher resolution and more accuracy, as well as the development of droplet-based pattern clustering and segmentation algorithms. However, maintaining a consistent droplet size and density distribution at the early stage of condensation phases is challenging and unresolved because the early stage is short (in millisecond scale), and the droplet growth rate in this phase is fast (in μm/s scale) [6].

In fact, the growth of droplet size has been successfully controlled in closed environmental systems. For instance, in environmental scanning electron microscopes (ESEM), the environmental conditions, including vapor temperature and relative humidity, can be controlled precisely; in doing so, the droplets can be controlled approximately in thermodynamic equilibrium by finely tuning the temperature of the substrate [7,8]. However, there is no feedback control of droplet size involved in ESEM. Meanwhile, ESEM is prohibitively expensive. Further, ESEM cannot be applied for pattern or surface inspection in real-time manufacturing processes because its close environmental setup cannot be adapted to general open manufacturing environments.

For monitoring of manufacturing quality in the open environmental system [6], the CFs are valid only for a very short time for pattern recognition and monitoring as shown in Fig. 1(b), because the parameters including relative humidity, pressure, and vapor flow rate were initially setup but not controlled. To transfer CFs to a long-time continuous manufacturing process for micron-scale pattern inspection in open environments (e.g., microcontact printing), we propose a cost-effective vision-based droplet measurement and feedback control method and integrate it into the optical surface inspection system. Vision-based measurements are widely used for automated and non-destructive applications and scenarios, such as motor bearing faults diagnosis [9], liquid impurity detection [10], circular fiber cross-section measurement [11], and surface deformation evaluation [12]. For the last decade, convolutional neural network (CNN)-based methods have overwhelmingly outperformed traditional techniques in vision tasks [13–15]. In this paper, we adopt a CNN in predicting the average droplet diameter in CFs in order to increase the droplet size prediction accuracy and reduce the computation time. The acquired droplet size is used for vapor flow rate control to achieve an equilibrium between evaporation and condensation phases. To our knowledge, this is the first time that droplet size and density are controlled in CFs by a machine-vision-based method in open environment surface inspection systems.

The rest of the paper is organized as follows. Section 2 reviews the related work about droplet size control and methods for circle detection. Section 3 describes the principles of the proposed vision-based droplet size control. Section 4 shows the hardware implementation of the high-resolution optical surface inspection system and experimental results. Section 5 concludes the paper.

2. Related work

2.1 Droplet size control

For open environmental CF systems, theoretical analysis shows that a sessile liquid drop is never in thermodynamic equilibrium and it will eventually evaporate in a saturated vapor atmosphere [8]. The time for macroscopic droplets to evaporate completely in saturated vapor pressure is so long that the nonequilibrium effects can be neglected. However, for surface inspection applications, the droplet diameter is in the micron-scale so the nonequilibrium cannot be neglected. Due to the nonequilibrium, it is then reasonable to control the droplet size in a desired range rather than a specific value. Practically, if the droplet size can be controlled below a threshold, and without coalescence, one can still acquire CFs that can be segmented precisely. Meanwhile, smaller droplet sizes will bring finer segmentation, pattern recognition, and measurement results [6].

2.2 Circle detection

The first step in droplet size control is measuring the actual droplet size. Several methods have been developed to measure the droplet size. These methods can be categorized into two groups: optical techniques, and intrusive probes. Optical techniques are the most robust droplet size measurement method with the advantage of non-intrusiveness. For optical techniques, the droplet size is measured from the captured images by applying image processing. A popular method for recognizing circles and calculating their diameters is the Circle Hough Transform (CHT) [1,6,11,16]. The circle candidates are produced by “voting” in the Hough parameter space and then selecting the local maxima in an accumulator matrix. However, for finding circle parameters such as the diameter and center, the standard CHT iterates through designated possible diameters, which needs a large storage requirement and is computationally expensive. In [17], a curvature aided Hough Transform for circle detection (CACD) is presented, which estimates the circle radius from curvatures. The experimental results in [17] show that CACD is 8 times faster than the standard CHT. In [18], a Circlelet Transform (CT) based circle detection method is proposed for red blood cell segmentation, which is more robust than the standard CHT when there are overlapped circles. However, the CT method needs prior knowledge of the number of circles.

These aforementioned methods are based on different transformations of the original images, while another type of circle detection is based on edge detection. In [19], a droplet imaging instrument is developed to study the liquid water content and the median volume diameter of water droplets. The system performs shadowgraph imaging using a high-speed digital camera and LED background illumination. The size of an imaged droplet is estimated by two steps: first, a Laplacian of Gaussian (LOG) edge detection filter is applied

to the image which could detect the edges of droplets, and then the cross-sectional area of each identified object is determined by counting the number of pixels in its filled boundary. From the cross-sectional area, the diameter is calculated. Besides optical imaging methods, the droplet size can be also measured based on light-scattering methods. A scattering method may be preferred when more detailed statistical properties of droplets, such as velocity, are desired [20].

One can also apply intrusive probes to characterize droplet behaviors. Such as in [21], an oil droplet size and velocity determination method using a fiber-optic reflectometer (FOR) was proposed. The velocity is measured from the light reflection of the oil droplet while the droplet is moving towards the fiber tip. The droplet diameter is calculated by multiplying the oil droplet velocity and the oil-phase residence time. The oil-phase residence time is determined using the moments of entry and exit of an oil droplet in the FOR-signal time series. Other intrusive probes, like conductivity probes [22], have also been applied in measuring droplet size and velocity. However, intrusive probes can only measure droplet size when the droplets are spherical or ellipsoidal, which may not be true in CFs.

3. Methods

3.1. Theory of condensation and evaporation

Depending on the wettability of the surface, the condensed vapor on a cooled surface has two different modes, dropwise mode and filmwise mode. Both condensation modes can be exploited for pattern recognition. An example is the visualization of CNTs: dropwise mode is used for imaging CNTs with impurities and filmwise mode is used for clean CNTs [4]. However, dropwise condensation is preferred in pattern recognition for SAMs. For dropwise condensation, three phases of droplet growth can be identified: (1) droplets initially nucleate on a cooled surface and grow with direct condensation; (2) as the droplets grow, adjacent droplets coalesce; and (3) new droplets nucleate in the space between big droplets. Based on the diffusion theory [23], the volume change of a sessile droplet with time t in the condensation phase can be described by

$$V = \left(\frac{3}{\pi\beta}\right)^{\frac{1}{2}} \left[\frac{4\pi DM}{3\rho RT} (P_{\infty} - P) f \right]^{\frac{1}{2}} t^{\frac{3}{2}} \quad (1)$$

with $\beta = (1 - \cos\theta)^2 (2 + \cos\theta)$ and

$$f = \frac{1}{2} (0.6366\theta + 0.09591\theta^2 - 0.06144\theta^3) \text{ for } \theta < 10^{\circ}$$

$$f = \frac{1}{2} (0.00008957 + 0.6338\theta + 0.116\theta^2 - 0.08878\theta^3 + 0.01033\theta^4)$$

for $\theta \geq 10^{\circ}$

where θ is the contact angle in radians, D is the diffusion coefficient in m^2/s , M is the molar mass in kg/mol , R is the gas constant in $\text{J}/\text{mol K}$, T is the temperature of the vapor in K , ρ is the fluid density in kg/m^3 , P_{∞} is the partial vapor pressure far away from the droplet in Pa , and P is the saturation vapor

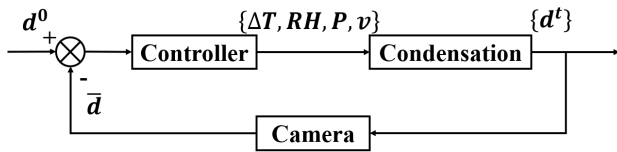


Fig. 2. Feedback control for consistent droplet size.

pressure at the droplet's surface in Pa. For evaporation, the volume change will follow equation

$$V^{2/3} = V_0^{2/3} - \frac{4\pi DM}{3\rho RT}(P - P_\infty) f\left(\frac{3}{\pi\beta}\right)^{1/3} t \quad (2)$$

where V_0 is the initial droplet volume in m^3 .

From Eqs. (1,2), it is clear that if the vapor pressure is larger than the saturated vapor pressure, the water vapor in the air will condense on the surface. On the contrary, the droplets will evaporate if the vapor pressure is less than the saturated vapor pressure. For the condensation process, the droplet will grow on the surface with a constant contact angle for specific surface materials. During the evaporation process, however, droplets can evolve in a great variety of modes, sometimes keeping their contact radii constant, sometimes keeping their contact angles constant, and sometimes neither of these parameters are kept constant (see more details in ref. [24]). Based on our experimental observations (see section 4.2 below), for droplet diameters smaller than $3.5 \mu\text{m}$, the droplets will condense and evaporate in a constant contact angle mode. We can thus assume constant contact angle mode both for condensation and evaporation.

For pattern recognition applications, small droplet size and dense droplet distribution will lead to smooth, precise, and accurate segmentation of surface patterns [1,6]. Hence, it is necessary to keep most of the droplets in the early growing phase via direct condensation before any coalescence events occur by controlling an equilibrium between condensation and evaporation. Note that for water condensation, the critical radius for nucleation is 1 nm to 100 nm [25]. As an optical imaging system has a lateral resolution limit (200 – 250 nm) due to the physics of diffraction, all the visible droplets in this paper are controlled in growing as close as possible to the nucleation phase.

3.2 Feedback control for consistent droplet size of CFs

In physical models of condensation and evaporation, the behaviors of droplets are governed by environmental variables, including the room temperature, relative humidity, vapor flow rate, and cooling temperature of the substrate. These variables are coupled which makes it difficult to maintain a stable droplet size using feedforward control. Moreover, in open environmental systems, there are random disturbances and uncontrollable effects on these variables, such as airflow caused by air conditioning systems, or the movement of human beings and machines. For example, when the web moves in roll-to-roll fabrications [6], it will induce additional airflow around the web thus changing the droplets' behaviors. However, based on the diffusion theory, as long as the vapor pressure is higher than the saturated vapor pressure,

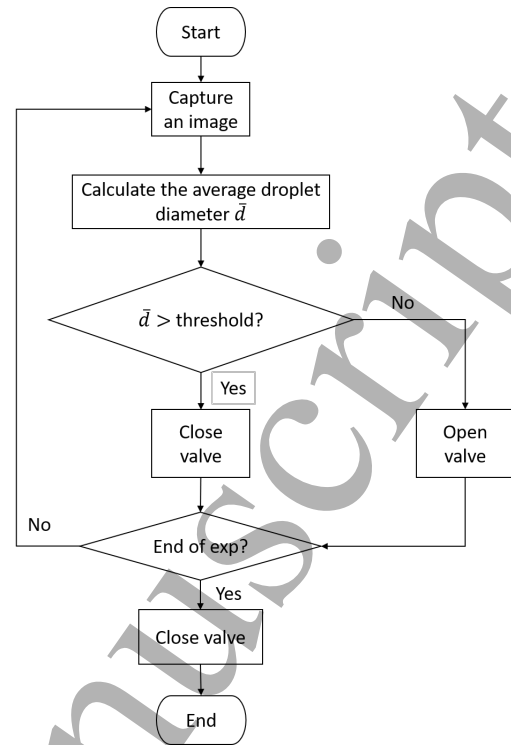


Fig. 3. Flowchart of the on-off controller.

the droplets will grow; if the vapor pressure is less than the saturated vapor pressure, the size will decrease, making it feasible to maintain the droplet sizes in a range.

Our basic idea is to tune the vapor flow of the evaporation and condensation phases for an equilibrium between the phases, and hence to achieve a consistent droplet size in CFs. Intuitively, if the droplet size is sufficiently large, reduce the vapor flow rate and let the droplets start to evaporate; before the droplets evaporate completely, increase the vapor flow rate, and let the droplets start to grow. This is reasonable for surface inspection applications because the patterns can still be segmented if the droplet size is visible and sufficiently smaller than the feature size on the surface.

Hence, we propose a feedback controller for consistent droplet size control of CFs. In an open condensation chamber, the condensation process has a vapor flow rate v around the target surface as an additional control parameter, besides the setup of ΔT , RH , and P . Here, ΔT is the temperature difference between vapor and substrate, RH is the relative humidity around the condensation surface, and P is the saturation vapor pressure directly at the droplet's surface. Mathematically, the average droplet size \bar{d} on the condensed surface for a specific material can be formulated as a control function of the four parameters as $\bar{d} = f(\Delta T, RH, P, v)$. Maintaining a consistent droplet size and density distribution can be achieved by the feedback closed loop in Fig. 2. Here, d^{t_i} denotes the diameter of the i^{th} droplet at time t . A fast-speed and high-resolution camera can capture the average droplet size \bar{d} in real-time when the condensation evolves with controlled parameters $(\Delta T, RH, P, v)$. In this paper, we select vapor flow rate v as the

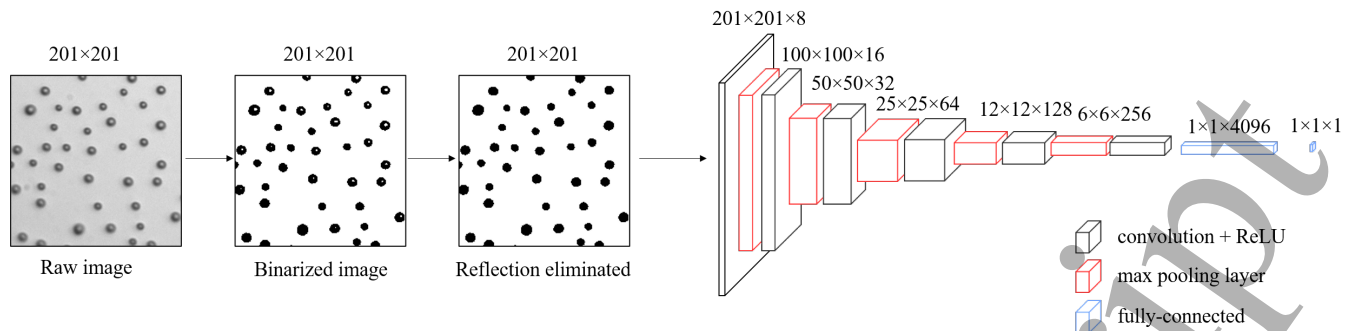


Fig. 4. Workflow of average droplet diameter calculation. The raw image is first binarized using Otsu's method, then the light reflection is eliminated by finding white pixels that are not connected to the background. Finally, the preprocessed image is fed into a customized CNN and the output of the CNN is the predicted average droplet diameter in the image.

manipulated variable and try to keep the remaining three variables as constant as possible to maintain a consistent precise droplet size on CFs.

In detail, a vision-based droplet size control method is developed as shown in Fig. 3. A threshold of the measured average droplet size is tuned to control the station of the valve. When the experiment starts, as the detected droplet size is smaller than the threshold, the valve opens and the droplets start growing. After the calculated average droplet size achieves the threshold, the valve will close immediately. Then the droplets will first keep growing for a short time due to the residual hot vapor and then they will begin to evaporate. In this case, we make sure that the overshoot of the average droplet size is minimized. After the average droplet size has become smaller than the threshold, the valve will open, and the droplets will grow again. From the surface inspection perspective, we want to control the average droplet size as small as possible while maintaining a high droplet density, which means the droplets cannot evaporate totally during the control process. Therefore, it is important to find a suitable threshold for the on-off controller. A detailed tuning result for the threshold is described in section 4.3. Meanwhile, the growth rate of droplet size can be affected by the flow rate, vapor temperature, and surface temperature. These parameters must be tuned carefully for various applications. If the flow rate is too high, the droplets would grow too fast such that the droplet would be bigger than the desired range in one control period. Meanwhile, the resulted high-speed vapor would also induce vibration to the substrate, which causes the camera to lose its focus. Regarding vapor temperature, temperatures that are too high may cause damage to the substrate and the patterns. When the droplet size achieves the upper bound of the size limit, the mass flow controller is closed immediately, and the droplets will start to evaporate to the ambient air. Similarly, due to the time delay, the upper bound should be smaller than the size where coalescence occurs. To ensure evaporation, the temperature of the substrate must be higher than the dew point of the ambient air. Also, for long-term operations, if the vapor generation system functions for a long time, it will increase the temperature and the relative humidity in the working space, which may be harmful to the manufacturing process. More seriously, if the air in the

working space is saturated with vapor, the evaporation process will not happen. Thus, an air conditioning system must be installed in the working space to maintain the temperature and relative humidity of the ambient air.

Based on the above analysis, the droplets on the surface would be controlled between condensation and evaporation periodically via the control of the mass flow controller and as a result, the droplets are maintained in a specific size range where neither complete evaporation nor coalescence occurs.

3.3. Droplet size prediction algorithm

Since the droplet size changes rapidly, the goal of the vision system is to capture the image, recognize droplets, and extract the average size from the image as fast as possible. Here, we propose an average droplet diameter prediction method using a CNN as shown in Fig. 4. Before fed into a CNN, the raw image is preprocessed by steps shown on the left of Fig. 4. First, the contrast-enhanced image is binarized based on Otsu's method [26] which can distinguish the background and the droplets. Then, the background is defined by finding the largest connected area. The light reflection is then eliminated by reversing all white pixels not connected to the background. After preprocessing, a well-trained CNN is used to predict the average droplet diameter. The detailed description of the customized CNN is as follows.

3.3.1. CNN architecture

In this section, the CNN architecture design is presented. In Fig. 4, after preprocessing (binarization and elimination), the input to the network is a single channel binary image, and the output is the predicted average droplet diameter. Intuitively the proposed task is a CNN-based regression process that is aimed to find the average droplet diameter in the binary image. Based on the comprehensive analysis of CNN-based regression [27], a general-purpose CNN architecture adequately tuned can yield results close to the state-of-the-art without having complex architectures. Therefore, we choose the three most referred CNN architectures in the recent literature as our baselines: VGG [28], U-Net [29], and ResNet [30]. U-Net has a large number of feature channels in the up-

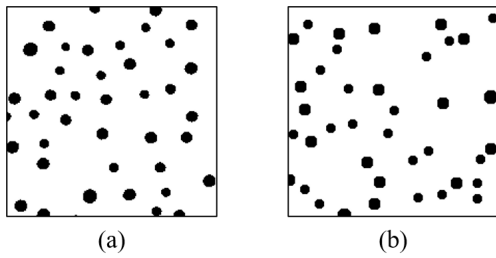


Fig. 5. Comparison between a real CF and an artificial CF. (a) Real CF. (b) Artificial CF.

sampling part, which makes the network an effective model for pixel-wise regression tasks. However, the detailed spatial information of the droplets is not needed for our task, and hence the up-sampling parts are redundant. If we get rid of the up-sampling parts, the architecture of U-Net degrades to a VGG-like network. The main novelty of ResNet is the use of identity shortcuts, which augment the network depth. ResNet addresses the popular degradation problem, which means a deeper ResNet has better accuracy. However, a deeper ResNet needs more computational time. For example, an 18-layer ResNet needs 7 ms to calculate the average droplet size for one image in our project (see Table 2), which is too long to be applied in real-time. For a shallower ResNet, the architecture is more complex than VGG architecture but has similar performance tendencies. Therefore, we develop a cost-effective architecture based on VGG for our specific task.

VGG net has been successful in many regression tasks, including depth prediction in digital holography [31], and 3D pose regression [32]. The basic architecture of the VGG net is a stack of several convolutional blocks followed by 3 fully connected layers. The convolutional block consists of one convolutional layer, a rectification non-linearity layer (ReLU), and a max-pooling layer. The most important feature in the VGG net is the small filter size (3×3) of the convolutional layer, which makes it feasible to adjust the depth of the network according to different tasks. In our task, we made several modifications to the VGG architecture. First, instead of using RGB image for input to the VGG, our input is a single channel 201×201 pixel² binary image so that the first convolution kernel size of our architecture is $3 \times 3 \times 1$ instead of $3 \times 3 \times 3$ in VGG. Second, we keep 6 convolutional layers to simplify the computation complexity. Third, we only keep one fully connected layer to reduce most of the network weights. Finally, we change the last layer into a regression layer to fit the continuous value output. The complete architecture of the proposed CNN is shown in the right of Fig. 4. We hypothesize that it is faster to optimize the modified VGG network than to optimize the three baseline architectures. The modified VGG net should also have less computation time and equivalent accuracy in the droplet size recognition than other existing methods.

3.3.2. Training and testing

Since the input images to the CNN are only simple binary circles, the training CF dataset can be artificially constructed. To use artificial CFs to mimic real CFs, three main factors

Table 1. Hyperparameters for Training Neural Networks

Optimizer	Learning rate	Epoch	Batch size	Momentum
SGDM	0.001	50	32	0.9

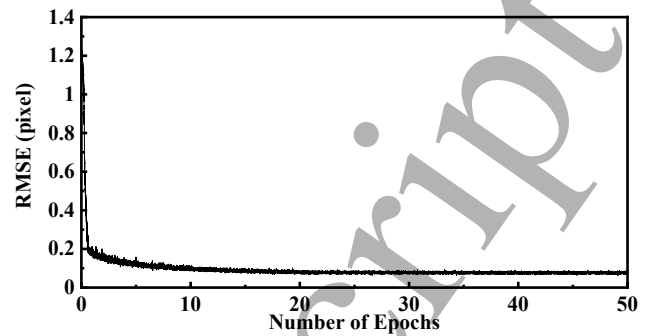


Fig. 6. Performance curve in terms of RMSE.

Table 2. Average Diameter Prediction Errors and Computational Time for the Proposed Method and Other Methods

Method	Error (pixels)	Runtime (ms) ^a
CNN (Proposed architecture)	0.23	0.34
CNN (VGG16)	0.40	3.78
CNN (U-Net)	0.45	17.44
CNN (ResNet18)	0.40	7.23
CHT	0.41	11.64
LOG	0.57	30.21
CACD	0.40	28.69
CT	0.23	264.35

^aRuntime stands for the computational time for one image.

Table 3. Training Time and FLOPs for Different CNN architectures

Architecture	Training time (hour) ^a	FLOPs
Proposed architecture	0.8	192 Million
VGG16	18	24 Billion
U-Net	30	62 Billion
ResNet18	16	45 Billion

^a Training was performed on MATLAB R2019a with dual NVIDIA® GeForce® RTX 2080 Ti graphics cards. Batch size is 32 and epoch is 50.

need to be decided: nucleation site distribution, droplet density, and droplet size distribution. A nucleation site distribution theoretically follows a random spatial Poisson distribution [33], which means the distance of the nearest-neighbor nucleation site follows the Poisson distribution. However, the substrate surface is vulnerable to contaminations in practical open environmental CFs, which can be problematic as vapor is more likely to condense on contaminated areas. Regarding the droplet density, experimental values were found in the range between 10^9 m⁻² and 10^{15} m⁻² [34]. For the substrates used in our experiments, the density of the droplets is observed in the range between 1.5×10^{10} m⁻² and 2.6×10^{10} m⁻², approximately resulting in 35 to 60 droplets on a 201×201 pixel² CF. Finally, regarding the droplet size distribution, the theoretical analysis in [35]

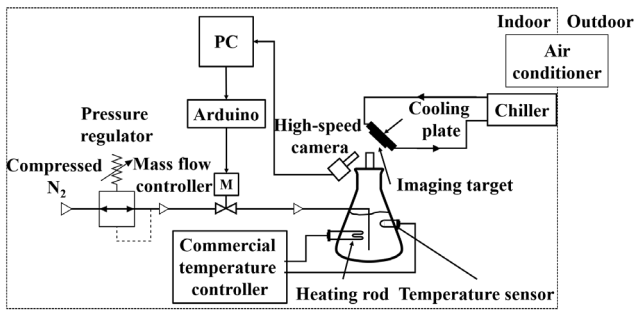


Fig. 7. Schematic diagram of surface inspection system based on CFs.

implies that when the droplet diameter is smaller than the interaction diameter (the interaction diameter is the diameter in which coalescence starts occurring), the droplet size is uniformly distributed. However, according to our experimental observations, the size distribution of droplets on contaminated substrate surfaces is no longer highly uniform but is instead correlated to the region of interest and the surface contamination levels. To obtain a training dataset that completely spans the workspace of the above three factors, we assume that impurities are equally possible to appear on any position on the surface. Therefore, the nucleation sites are generated following a uniform distribution on the image. The diameters of the droplets are randomly distributed between 6 pixels and 18 pixels. The number of droplets is selected between 30 and 70 with an interval of 5 on an image of 201×201 pixel². For each droplet number, 10000 images are generated. Therefore, there are 90000 images generated in total and each image is labeled with the corresponding average diameter. Figure 5 shows the similarity between the real CF and the artificial CF.

Since the output of the CNN is a scalar, which is the predicted average diameter of each input image, the mean-square error is selected for the loss function. The combination of training hyperparameters selection is shown in Table 1. The training takes approximately 50 minutes in a MATLAB R2019a environment with Intel(R) Core (TM) i9-9900X CPU @ 3.50 GHz with two NVIDIA® GeForce® RTX 2080 Ti graphics cards. Figure 6 shows the performance of root-mean-square error (RMSE) in the training phase.

For the test, 10000 new images are generated with random droplet numbers and random droplet sizes. The average error and runtime for an individual image are shown in Table 2. The error is measured in terms of RMSE. We have compared 4 traditional circle detection methods with the proposed CNN-based method, including the standard CHT, CACD, CT, and an edge detection method. For the edge detection method, we use the same LOG edge detection method as described in [19]. Here, we abbreviate this edge detection method as LOG. To prove the superiority of the proposed CNN architecture, we also train the standard VGG16, U-Net, and ResNet18 for comparison. The training hyperparameters are the same as the proposed CNN network.

As seen in Table 2, the proposed CNN architecture is the fastest and most accurate method. The larger error of the standard CHT method can be attributed to its overestimation

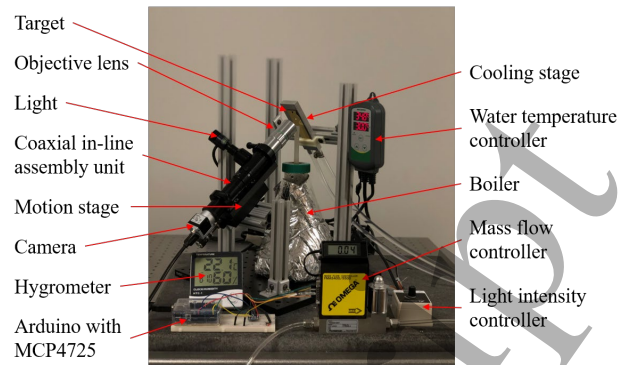


Fig. 8. Experimental setup of the high-resolution optical surface inspection system.

of the average droplet diameter because it may miss certain droplets when droplet diameters are smaller than 10 pixels. Additionally, since CHT iterates through all designated possible diameters, it is slower than the proposed CNN method. For the LOG method, the error mainly results from the stair-like edge of a droplet on the image. For example, if the designed diameter of a droplet is 10 pixels, the actual area of the droplet is 69 pixels on the image and the calculated diameter is 9.37 pixels. Furthermore, LOG measures the 2nd spatial derivative of the image which is 100 times slower than the proposed CNN method. The CACD has a similar runtime with LOG and is slightly more accurate than LOG. The CT achieves the same accuracy as the proposed CNN architecture, but it needs 264.35 seconds to get the average diameter which is not suitable for real-time applications. Regarding other CNN architectures, more analysis is carried out in Table 3. Here FLOPs represent the floating-point operations which can be used to reflect the complexity of the models. As shown in Table 3, the simplified VGG net can effectively improve the computational efficiency and reduce the model complexity, while maintaining high accuracy. Consequently, our proposed method outperforms all the other methods for droplet size calculation.

4. Experimental results and discussion

4.1 Setup of the high-resolution optical surface inspection system

A high-resolution optical surface inspection system integrated with the proposed droplet size control method was set up. Figure 7 shows the schematic diagram of the high-resolution optical surface inspection system.

It consists of three subsystems: a warm saturated air generator, an imaging system, and a water-cooling substrate. The warm saturated air generator is made from a plastic Erlenmeyer flask wrapped up by heat barriers. A heating rod and a temperature sensor (ITC-308, Inkbird) work together to maintain a constant temperature of the deionized (DI) water in the flask. Dry nitrogen gas is humidified in the flask and is blown toward the substrate through a nozzle made from a plastic tube that is 50.8 mm long with a 6.35 mm inner diameter. The flow rate of the humidified nitrogen gas is

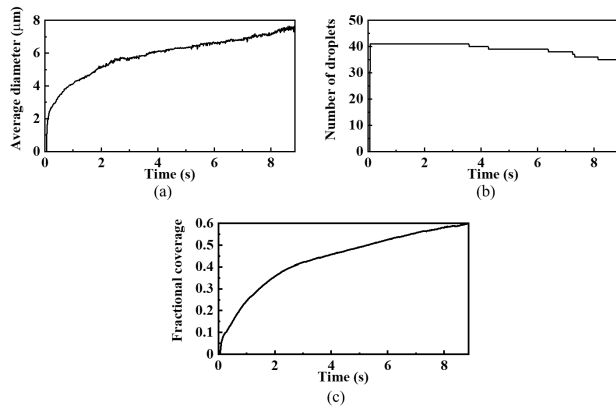


Fig. 9. Time evolution of droplet size and number, and fractional coverage for dropwise condensation on gold surface that were exposed to continuous saturated vapor. (a) Average droplet diameter evolution. (b) Droplet number evolution. (c) Fractional coverage evolution of droplets.

regulated by a mass flow controller (FMA5400, 0-2 SLM, Omega). Since the mass flow controller works under analog signals, an Arduino with 12-Bit DAC chip MCP4725 is used as an intermedia between the PC and the mass flow controller. The imaging target is attached to a homemade chiller cooled by flowing DI water of 22 °C. The imaging system consists of a fast-speed CMOS area-scan camera (acA1300-200um, Basler), a motion stage (PT1A, Thorlabs), a coaxial lighting source (SL112, Advanced illumination), a coaxial in-line assembly unit (infinitiTube™ Standard, Infinity Photo-Optical), and an objective lens (Mitutoyo). At 20× magnification, the pixel size in the acquired images is 0.24 μm/pixel and the imaging resolution is 0.7 μm. A polarizing filter is inserted in the coaxial in-line assembly unit to reduce the reflections of the droplet surface and enhance the image contrast. The coaxial light is adjusted manually by a light intensity controller (ICS2, Advanced illumination).

Figure 8 shows the front view of the test platform. To reduce the vibration effects on the imaging results, the test platform is assembled on an optical table. The camera and lens face up to the substrate to avoid contamination on the lens by fogging. For the same reason, the outlet of the nozzle is fixed as close as possible to the substrate while keeping away from the imaging path. A hygrometer is used to monitor the relative humidity and temperature in the room.

4.2 Time-dependent evolution of condensation growth process

Figure 9 shows the time-dependent evolution of the condensation growth process without droplet size control, including the average droplet diameter, droplet density, and fractional coverage which is the ratio of the cumulative “wetted” area covered by droplet footprints to the range of interest area where condensation occurs. The flow rate of nitrogen is controlled at 1 slm, the water temperature is set to 30 °C, and the temperature of the cooling system is 22 °C.

Theoretically, a clean gold surface is hydrophilic, and the contact angle is 0 degrees which means the condensation of vapor would form a thin film [36,37]. However, since the

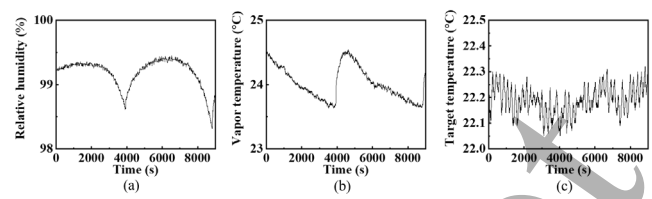


Fig. 10. Long-term measurements of controlled variables in the proposed system. (a) Relative humidity near the outlet of the nozzle. (b) Vapor temperature near the outlet of the nozzle. (c) Temperature of the cooling target.

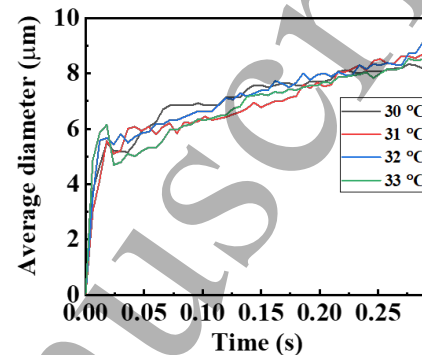


Fig. 11. Average droplet diameter evolution for different water temperatures.

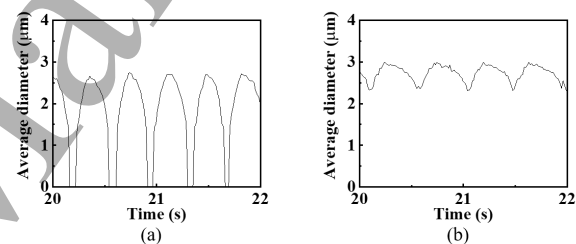


Fig. 12. Droplet size control threshold tuning process. (a) Droplet size control performance when threshold is 2 μm. (b) Droplet size control performance when threshold is 2.5 μm.

surface energy for clean gold surfaces is high, the gold surface will adsorb organic contaminants of low surface energy when exposed to the environment. The formed contaminant layer will lower the surface energy of the gold surface and lead to an increase in the contact angle, thus resulting in a dropwise CF. For a different thickness of the contaminant layer, the gold surface would have a different wettability. To make the results consistent, the gold surface is treated by solvent cleaning before each experiment. Solvent cleaning consists of four phases. First, the gold slide is immersed in an ultrasonic bath of acetone for 5 minutes, followed by an ultrasonic bath of ethanol for 5 minutes, then an ultrasonic bath of deionized water for 5 minutes, and finally, blown dried with clean compressed nitrogen.

Figure 9(b) clearly shows that coalescence starts occurring at 3.5 s and the corresponding average droplet diameter is about 5.76 μm. For imaging applications, a larger density of droplets in CFs can lead to more detailed patterns. Hence, the droplets should be controlled in the first growing phase when

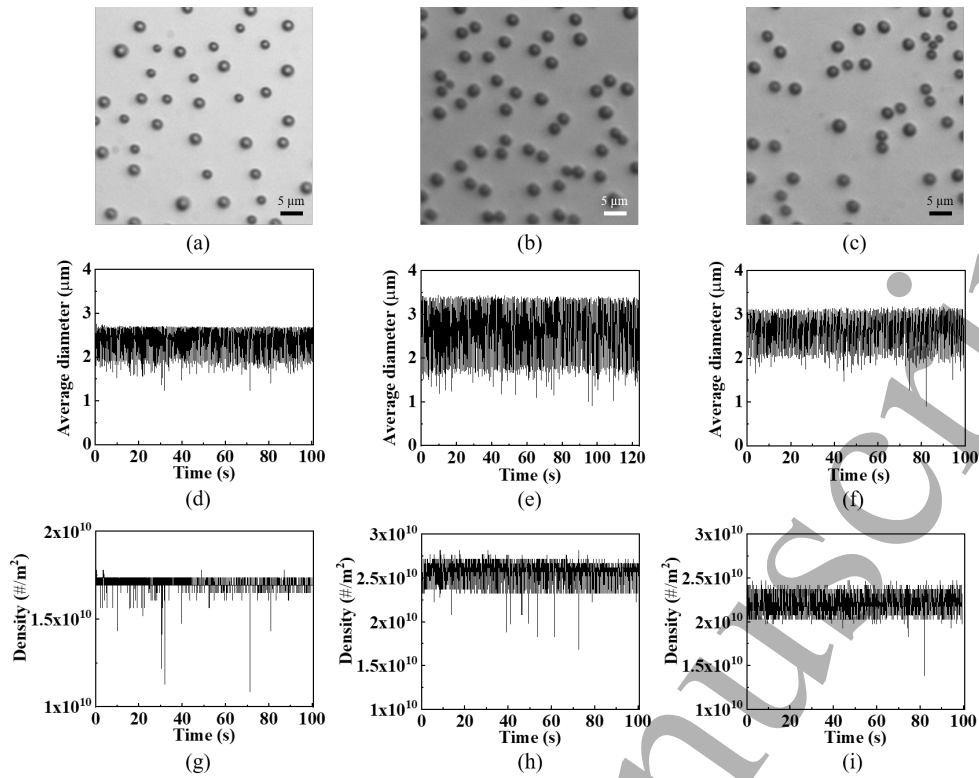


Fig. 13. Droplet size control performance on different metal substrates. (a) A typical CF on gold substrate. (b) A typical CF on aluminum substrate. (c) A typical CF on copper substrate. (d) Droplet size control performance on gold substrate. (e) Droplet size control performance on aluminum substrate. (f) Droplet size control performance on copper substrate. (g) Droplet density control performance on gold substrate. (h) Droplet density control performance on aluminum substrate. (i) Droplet density control performance on copper substrate.

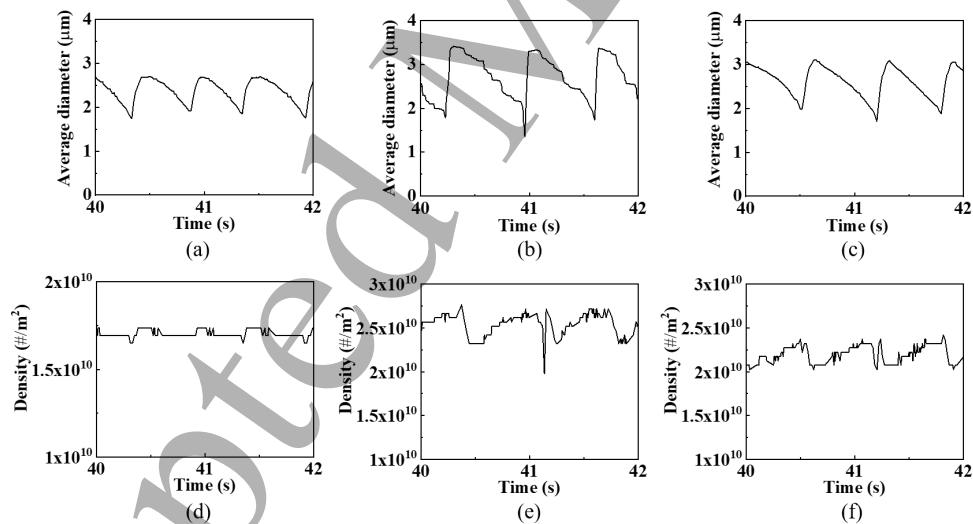


Fig. 14. Droplet size control performance on different metal substrates in the time scale of control loop rate (14.32 ms). (a) Droplet size control performance on gold substrate. (b) Droplet size control performance on aluminum substrate. (c) Droplet size control performance on copper substrate. (d) Droplet density control performance on gold substrate. (e) Droplet density control performance on aluminum substrate. (f) Droplet density control performance on copper substrate.

the droplets grow via direct vapor condensation and not coalesce. For the gold substrate, it is then reasonable to control the droplet diameter in the range that is smaller than 5 μm where no coalescence events occur.

Table 4. Runtime and Percent Time for Key Routines in the Proposed Droplets Size Control Method

Routine	Runtime (ms)	Percent time (%)
Image acquisition	1.67	11.66
Image preprocessing	3.58	25.00
Average droplet size prediction	0.34	2.37
Command transmission	8.73	60.96

As stated in section 3.2, we select the flow rate as the manipulated variable to control the average droplet size. It is necessary to clarify that the other three parameters (ΔT , RH , P) are constant. Note that P is only dependent on the target temperature. Figure 10 shows the measured RH , the vapor temperature, and the target temperature near the outlet of the nozzle using a digital humidity and temperature sensor (SHT11, SENSIRION). We can find that based on the experimental setup, the RH can be maintained with values larger than 98% as shown in Fig. 10(a). The variations of the vapor temperature and the target temperature are less than 0.5 °C and 0.2 °C as shown in Fig. 10(b, c), respectively. Since the commercial water temperature controller uses on-off control, the RH and the vapor temperature change periodically as shown in Fig. 10(a, b). Hence, it is necessary to study the effects on the droplet size evolution by the fluctuations of RH and the vapor temperature. Since the fluctuations are caused by the change of water temperature, we record the droplet size evolution curves for different temperatures from the readings of the water temperature sensor. We found that when setting the water temperature to 30 °C, the water temperature will change from 30 °C to 33 °C periodically. Therefore, we record the average droplet size evolution data for temperature from [30 °C, 31 °C, 32 °C, 33 °C] as shown in Fig. 11. We can find that there is no large difference among the evolution curves. Hence, it is reasonable to select the flow rate as the manipulated variable for the droplet size control.

4.3 Droplet size control on different substrates

According to the control algorithm described in section 3.2, we use an on-off controller to control the average droplet size. For the on-off controller, there is only one parameter required to be tuned which is the threshold to open or close the valve. Since we want to control the average droplet size as small as possible, we experimentally increase the threshold starting from 0. Figure 12(a) shows the droplet size control performance on gold substrate when the threshold is 2 μm . It can be seen that the droplets disappear during the control process which means the threshold is still too small. We find that when setting the threshold to 2.5 μm , acceptable performance is obtained where the droplets maintain a high density and have an average droplet size smaller than 3.5 μm . Meanwhile, we find that for different substrates, the minimum reasonable thresholds are different due to the different wettabilities. Therefore, for different substrates, the threshold should be tuned according to the above procedure.

Figure 13 shows the performance of droplet size control on different metal substrates. All the tested substrates were rinsed

following the procedure described in section 4.2. Since we use an on-off controller, the controlled size is oscillating. However, the average droplet size is controlled to be smaller than 3.5 μm , which is smaller than 5 μm and in the acceptable range as declared above. Additionally, we also calculate the density of droplets using the standard CHT shown in Fig. 13 (g-i). Even though the density is not directly controlled by the proposed system, it can be maintained in an acceptable range with trivial variation because the density is highly correlated with the droplet size. The resulted small droplet size and dense droplet distribution will lead to smooth, precise, and accurate segmentation of surface patterns.

Meanwhile, the rate of the control loop is approximately 14.32 ms, which includes image acquisition, image processing, average droplet size prediction, and command transmission. Figure 14 shows the typical fluctuations of the droplet size and density at the time scale of the control loop rate. It can be found that the control loop rate is acceptable because it is much faster than periods of fluctuations, which are more than 0.5 s. Additionally, we can find that the droplets' condensation time is shorter than the evaporation time during each control loop. The reason is that when the mass flow controller opens, the saturated vapor is blown to the target by the compressed nitrogen in a short time and the droplets start to grow in a saturated vapor. However, when the mass flow controller closes, the saturated vapor around the target gradually diffuses to the ambient air, which causes the average evaporation rate to be slower than the condensation rate. Nevertheless, the typical condensation time measured in our experiments is about 100 ms, which is 7 times as long as the control loop rate. We also calculate the respective time for each routine in one control loop as shown in Table 4. The most time-consuming routine is the communication between PC and Arduino, which consumes up to 60% of the entire control loop time. The latency is caused by the communication protocol between PC and Arduino. One way to speed up the command transmission is to integrate the control system into a real-time control system, such as NI CompactRIO. NI CompactRIO is a combination of a real-time controller, reconfigurable IO modules, and an FPGA module. The analog voltage output module can be easily integrated and controlled by the real-time controller through the FPGA module. In this way, the command transmission time can be reduced to below 1 ms.

4.4 Real-time imaging of CFs on HDT-gold print patterns

One critical application of CFs is the visualization of patterned SAMs on gold for microcontact printing [6]. Microcontact printing is a form of soft lithography and is a leading candidate for full-scale commercial production of micro or nanopatterned surfaces for a variety of applications. The process of microcontact printing involves the transfer of SAMs from patterned elastomer stamps to metal substrates. If SAMs formed on metal substrates serve as an etch resist, then the process is called negative microcontact printing [38]. The typical SAMs in negative microcontact printing are formed by

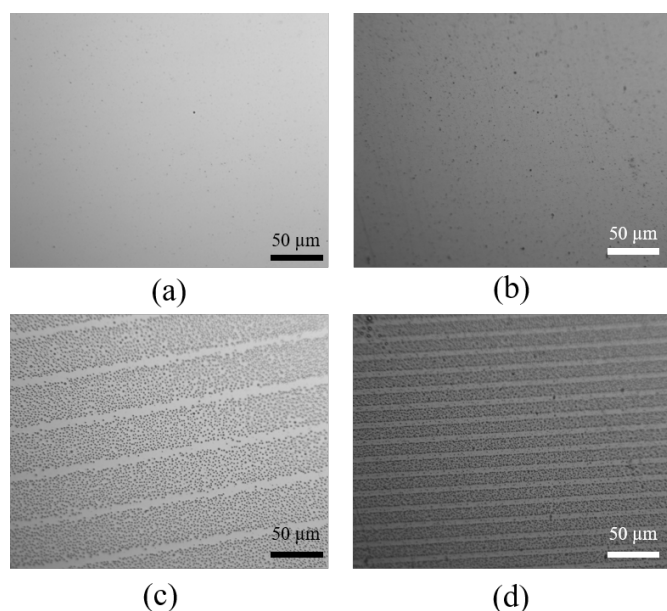


Fig. 15. CFs obtained on HDT and gold surfaces. (a, b) Optical images of the pristine patterns. (c) A CF of HDT patterns with 5 μm width and 50 μm spacing. (d) A CF of HDT patterns with 5 μm width and 20 μm spacing.

alkanethiols on gold surfaces. The gold surface protected by alkanethiols is the printed pattern and the remainder is etched out. For in-process control of microcontact printing, the ability to visualize the thiol-gold pattern immediately after printing and before etching is necessary for monitoring the printing quality. For instance, if there are disturbances to the printing process, such as damages to the elastic stamp or dirt on the stamp, the patterned SAMs would have certain deformation. If the deformation can be detected once it occurs, then the control system could respond immediately to the abnormal situations and thus lower the waste. Note that the alkanethiols used in microcontact printing are rather expensive, such as Hexadecanethiol (HDT), which can cost upwards of \$500/g. To test the proposed method in imaging patterned SAMs on gold, two types of patterns are generated using HDT. The patterns are grating patterns with the same line width of 5 μm and different spacing of 20 μm and 50 μm , respectively. Figure 15 shows the CFs of HDT-Gold print patterns. The images are full frames acquired using our imaging system, which covers a $307 \times 246 \mu\text{m}^2$ field of view. Figure 15(a, b) shows that the pristine HDT-Gold patterns are invisible under optical cameras. Since the gold surface is more hydrophilic than the surface covered by HDT, the droplets are more likely to condense on gold during condensation. Due to the droplet size control method, the droplets formed on the substrate are dense and small as shown in Fig. 15(c, d), which makes the HDT patterns distinguishable from the gold surface. Here we selected images in extreme situations where there are nearly no droplets formed on HDT. The droplets can be then clustered and segmented by our algorithm developed previously [6]. The segmented patterns can be then compared with the ground truth to monitor the printing quality.

5. Conclusion

A high-resolution optical surface inspection system based on droplet-size-controlled CFs is proposed in this paper. The real-time control of the average droplet size is carried out by on-off control of the warm vapor flow blown to the metal surfaces according to the fast calculation of average droplet size on CFs. To speed up the calculation of the average droplet diameter, a CNN is designed and trained. Testing results show that the proposed CNN architecture is faster and more accurate than conventional methods in calculating the average droplet size, including CHT, LOG, CADA, and CT in calculating the average droplet diameter. Experimental results on different metal substrates show that our method can control the average droplet diameter smaller than 3.5 μm and maintain consistent average droplet size and average droplet density distribution. Experiments of imaging printed SAM patterns on gold shows that this system can recognize patterns of the size of 5 μm which offers a potential solution to real-time measurement of the printed micro-scale patterns before applying the etching process to microcontact printing. Additionally, this high-resolution optical surface inspection system is not limited to the application of imaging SAM patterns, it can be also applied to other surface inspection tasks, including imaging of 2D materials, proteins, and anticounterfeiting.

Moreover, we found that the brightness of the image influences the droplet size calculation. The reason is that for dark ground, the contrast between droplets and the metal surface is weak which causes the shape of droplets on the processed image to become non-circular. An integrated automatic brightness adjusting system could be studied in the future. Meanwhile, we used a simple on-off control method in maintaining the droplet size. A learning-based predictive control method could be studied in the future.

Acknowledgments

This work was supported by the National Science Foundation under Grant CMMI-1916866 and Grant CMMI-1942185.

References

- [1] Merian C, Du X, Hardt D and AlQahtani H 2016 Roll-to-Roll Microcontact Printing of Flexible Aluminum Substrates Using Octadecylphosphonic Acid (ODPA) ASME 2015 International Mechanical Engineering Congress and Exposition (American Society of Mechanical Engineers Digital Collection)
- [2] Lopez G P, Biebuyck H A, Frisbie C D and Whitesides G M 1993 Imaging of features on surfaces by condensation figures *Science* **260** 647–9
- [3] Wang J, Li T, Xia B, Jin X, Wei H, Wu W, Wei Y, Wang J, Liu P, Zhang L, Li Q, Fan S and Jiang K 2014 Vapor-Condensation-Assisted Optical Microscopy for Ultralong Carbon Nanotubes and Other Nanostructures *Nano Lett.* **14** 3527–33
- [4] Xia K, Jian M, Zhang W and Zhang Y 2016 Visualization of Graphene on Various Substrates Based on Water Wetting Behavior *Adv. Mater. Interfaces* **3** 1500674

- [5] Du X, Wang J, Cui H, Tang T and Wu T 2016 Vapor-condensation-assisted reverse display for anti-counterfeiting applications *2016 IEEE 11th Annual International Conference on Nano/Micro Engineered and Molecular Systems (NEMS)* 2016 IEEE 11th Annual International Conference on Nano/Micro Engineered and Molecular Systems (NEMS) pp 316–9
- [6] Du X, Hardt D and Anthony B 2020 Real-Time Imaging of Invisible Micron-Scale Monolayer Patterns on a Moving Web Using Condensation Figures *IEEE Trans. Ind. Electron.* **67** 4077–87
- [7] Jung Y C and Bhushan B 2008 Wetting behaviour during evaporation and condensation of water microdroplets on superhydrophobic patterned surfaces *J. Microsc.* **229** 127–40
- [8] Butt H-J, Golovko D S and Bonaccorso E 2007 On the Derivation of Young's Equation for Sessile Drops: Nonequilibrium Effects Due to Evaporation *J. Phys. Chem. B* **111** 5277–83
- [9] Wang X, Guo J, Lu S, Shen C and He Q 2017 A computer-vision-based rotating speed estimation method for motor bearing fault diagnosis *Meas. Sci. Technol.* **28** 065012
- [10] Kragh M, Bjerge K and Ahrendt P 2016 3D impurity inspection of cylindrical transparent containers *Meas. Sci. Technol.* **28** 017002
- [11] Huang S, Jin W, Ye M, Liu Z, Yu B, Ying Y, Zhang X and Mu Y 2020 A vision based method for automated measurement of circular fiber cross-sections *Measurement* **162** 107913
- [12] Zhu C, Wang H, Kaufmann K and Vecchio K S 2020 A computer vision approach to study surface deformation of materials *Meas. Sci. Technol.* **31** 055602
- [13] Han T, Zhang L, Yin Z and Tan A C C 2021 Rolling bearing fault diagnosis with combined convolutional neural networks and support vector machine *Measurement* **177** 109022
- [14] Zhao J, Yang S, Li Q, Liu Y, Gu X and Liu W 2021 A new bearing fault diagnosis method based on signal-to-image mapping and convolutional neural network *Measurement* **176** 109088
- [15] Rifai A P, Aoyama H, Tho N H, Md Dawal S Z and Masruoh N A 2020 Evaluation of turned and milled surfaces roughness using convolutional neural network *Measurement* **161** 107860
- [16] Ballard D H 1981 Generalizing the Hough transform to detect arbitrary shapes *Pattern Recognit.* **13** 111–22
- [17] Yao Z and Yi W 2016 Curvature aided Hough transform for circle detection *Expert Syst. Appl.* **51** 26–33
- [18] Sarrafzadeh O, Dehnavi A M, Rabbani H, Ghane N and Talebi A 2015 Circllet based framework for red blood cells segmentation and counting *2015 IEEE Workshop on Signal Processing Systems (SiPS)* 2015 IEEE Workshop on Signal Processing Systems (SiPS) pp 1–6
- [19] Rydholm S and Thörnberg B 2016 Liquid Water Content and Droplet Sizing Shadowgraph Measuring System for Wind Turbine Icing Detection *IEEE Sens. J.* **16** 2714–25
- [20] Fujisawa N, Hosokawa A and Tomimatsu S 2003 Simultaneous measurement of droplet size and velocity field by an interferometric imaging technique in spray combustion *Meas. Sci. Technol.* **14** 1341–9
- [21] Do J, Chuang W-L and Chang K-A 2020 Oil droplet sizing and velocity determination using a fiber-optic reflectometer *Meas. Sci. Technol.* **31** 065301
- [22] Zhai L-S, Bian P, Gao Z-K and Jin N-D 2016 The measurement of local flow parameters for gas–liquid two-phase bubbly flows using a dual-sensor probe array *Chem. Eng. Sci.* **144** 346–63
- [23] Sokuler M, Auernhammer G K, Liu C J, Bonaccorso E and Butt H-J 2010 Dynamics of condensation and evaporation: Effect of inter-drop spacing *EPL Europhys. Lett.* **89** 36004
- [24] Stauber J M, Wilson S K, Duffy B R and Sefiane K 2014 On the lifetimes of evaporating droplets *J. Fluid Mech.* **744**
- [25] Liu X and Cheng P 2015 Dropwise condensation theory revisited: Part I. Droplet nucleation radius *Int. J. Heat Mass Transf.* **83** 833–41
- [26] Otsu N 1979 A Threshold Selection Method from Gray-Level Histograms *IEEE Trans. Syst. Man Cybern.* **9** 62–6
- [27] Lathuilière S, Mesejo P, Alameda-Pineda X and Horaud R 2020 A Comprehensive Analysis of Deep Regression *IEEE Trans. Pattern Anal. Mach. Intell.* **42** 2065–81
- [28] Simonyan K and Zisserman A 2015 Very Deep Convolutional Networks for Large-Scale Image Recognition *ArXiv14091556 Cs*
- [29] Ronneberger O, Fischer P and Brox T 2015 U-Net: Convolutional Networks for Biomedical Image Segmentation *Medical Image Computing and Computer-Assisted Intervention – MICCAI 2015 Lecture Notes in Computer Science* ed N Navab, J Hornegger, W M Wells and A F Frangi (Cham: Springer International Publishing) pp 234–41
- [30] He K, Zhang X, Ren S and Sun J 2016 Deep Residual Learning for Image Recognition *2016 IEEE Conference on Computer Vision and Pattern Recognition (CVPR)* 2016 IEEE Conference on Computer Vision and Pattern Recognition (CVPR) pp 770–8
- [31] Shimobaba T, Kakue T and Ito T 2018 Convolutional Neural Network-Based Regression for Depth Prediction in Digital Holography *2018 IEEE 27th International Symposium on Industrial Electronics (ISIE)* 2018 IEEE 27th International Symposium on Industrial Electronics (ISIE) pp 1323–6
- [32] Mahendran S, Ali H and Vidal R 2017 3D Pose Regression Using Convolutional Neural Networks *2017 IEEE International Conference on Computer Vision Workshops (ICCVW)* 2017 IEEE International Conference on Computer Vision Workshops (ICCVW) pp 2174–82
- [33] Enright R, Miljkovic N, Dou N, Nam Y and Wang E N 2013 Condensation on Superhydrophobic Copper Oxide Nanostructures *J. Heat Transf.* **135**
- [34] Liu X and Cheng P 2015 Dropwise condensation theory revisited Part II. Droplet nucleation density and condensation heat flux *Int. J. Heat Mass Transf.* **83** 842–9
- [35] Zhang L, Xu Z, Lu Z, Du J and Wang E N 2019 Size distribution theory for jumping-droplet condensation *Appl. Phys. Lett.* **114** 163701
- [36] Smith T 1980 The hydrophilic nature of a clean gold surface *J. Colloid Interface Sci.* **75** 51–5
- [37] Forrest E, Schulze R, Liu C and Dombrowski D 2015 Influence of surface contamination on the wettability of heat transfer surfaces *Int. J. Heat Mass Transf.* **91** 311–7
- [38] Delamarche E, Geissler M, Wolf H and Michel B 2002 Positive Microcontact Printing *J. Am. Chem. Soc.* **124** 3834–5